

# ULRR

## Tuning anatase to rutile ratio in nanocrystalline titania enriched from sustainable beach-sand from Cox's Bazar, Bangladesh

Item Type	Article
Authors	Roy, Oishy;Bashar, M S;Tofail, Syed Ansar;Haq, Ehtsham Ul;Gulshan, Fahmida
Citation	Surface and Interface Analysis, 2023, 55(6-7), pp. 526-535
Publisher	Wiley and Sons Ltd
Download date	2026-04-21 23:24:57
Item License	<a href="https://creativecommons.org/licenses/by-nc-sa/4.0/">https://creativecommons.org/licenses/by-nc-sa/4.0/</a>
Link to Item	<a href="https://doi.org/10.34961/researchrepository-ul.24118938">https://doi.org/10.34961/researchrepository-ul.24118938</a>

Roy Oishy (Orcid ID: 0000-0002-3768-1378)

Bashar M. S. (Orcid ID: 0000-0001-9793-4384)

Gulshan Fahmida (Orcid ID: 0000-0001-8803-259X)

## **Tuning Anatase to Rutile Ratio in Nanocrystalline Titania Enriched from Sustainable Beach-Sand from Cox's Bazar, Bangladesh**

Oishy Roy<sup>1</sup>, M. S. Bashar<sup>2</sup>, Syed A.M. Tofail<sup>3</sup>, Ehtsham Ul Haq<sup>3</sup>, Fahmida Gulshan<sup>1\*</sup>

<sup>1</sup>Dept. of Materials and Metallurgical Engineering, Bangladesh University of Engineering and Technology, Dhaka-1000, Bangladesh

<sup>2</sup>Bangladesh Council of Scientific and Industrial Research, Dhaka-1205, Bangladesh

<sup>3</sup>Department of Physics and Bernal Institute, University of Limerick, Ireland

Corresponding author: [fahmidagulshan@mme.buet.ac.bd](mailto:fahmidagulshan@mme.buet.ac.bd)

### **Abstract**

A sustainable source of titania (TiO<sub>2</sub>) is important in applications of photovoltaic devices, photocatalysts, sensors etc. Beach sand from Cox's Bazar, Bangladesh can be an excellent sustainable source of this titania as almost a quarter of it contains titania in the form of rutile and ilmenite. This study demonstrates the success of a sulfuric acid-based hydrometallurgical process in enriching titania in Cox's Bazar Beach Sand. The route produces precursors that can be conveniently calcined into nanocrystalline phase-pure anatase or anatase/rutile composites. We used both bulk and surface characterization to determine phase purity, crystallite size as well as surface chemistry and morphology of the resulting anatase and rutile/anatase mixture. The proportion of anatase/rutile can be tuned by varying digestion times. This hydrometallurgical route can potentially lead to the scalable production of precursors used in producing high-performance nanocrystalline titania from a sustainable source of beach sand from Cox's Bazar of Bangladesh.

**Keywords:** Titania enrichment; Sustainable raw materials; Cox's Bazar beach sand; Digestion; XPS

This article has been accepted for publication and undergone full peer review but has not been through the copyediting, typesetting, pagination and proofreading process which may lead to differences between this version and the Version of Record. Please cite this article as doi: 10.1002/sia.7201

## 1. INTRODUCTION

Titanium dioxide has been dominating the industries of paint, plastics, papers, cosmetics, porcelain, textile, inks etc. along with different photocatalytic applications and photoelectrochemical devices<sup>1-3</sup>. Titanium (Ti) in its metallic or oxide form has been extracted from their mineral forms such as rutile ( $\text{TiO}_2$ ) ilmenite ( $\text{FeTiO}_3$ ) and leucoxene ( $\text{Fe}_2\text{O}_3 \cdot n\text{TiO}_2$ )<sup>4</sup>. Ilmenite can partially convert in finely crystalline rutile in leucoxene<sup>5</sup> or fully convert into rutile mineral. Rutile is a high-grade mineral source for Ti but deposits containing more than 1% rutile have been becoming scarce due to continuous exploitation<sup>6</sup>. Alternative sources such as Ilmenite, titanium slag or synthetic rutile have been used by industries as intermediates<sup>4</sup>. Surface and bulk characterization of the quality and yield of the extracted and processed titania from these sources are important for further processing, quality control and valorizations of alternative sources and is the focus of the present study.

Bangladesh has heretofore unexploited reserves of titania minerals such as rutile (97,000 metric tons), leucoxene (70,000 metric tons) and ilmenite (1025,000 metric tons) in a total of 17 identified sand deposits. A total of 6 of these identified deposits are located along the Cox's Bazar – Teknaf coast<sup>7</sup>. These deposits are rutile rich with an average of ~2% rutile containing 90%  $\text{TiO}_2$  and compounds of zirconium (Zr), iron (Fe), silicon (Si), sulfur (S), aluminum (Al) and niobium (Nb) making up the balance. Importantly, these beach sands contain both 2.3% leucoxene with 65%  $\text{TiO}_2$ , and ~26% ilmenite containing 43%  $\text{TiO}_2$  respectively. Compounds of Fe, Si, phosphorus (P), manganese (Mn), and chromium (Cr) make the balance<sup>7</sup>.

High grade titania sources containing rutile are usually purified using chlorination due to its simplicity and high-quality product<sup>5,8</sup>. For lower or intermediate grade source such as ilmenite either pyrometallurgical or hydrometallurgical extraction routes are used<sup>9</sup> with some modifications<sup>10-15</sup>. Variation of pretreatment steps including roasting, smelting, decomposition, mechanical activation etc. also gave rise to much higher efficiency upgradation processes<sup>16</sup>. Multiple steps of thermo-reductive conversion and leaching make these processes costly and high energy intensive. On the other hand, hydrometallurgical processes using sulfate<sup>17-19</sup>, caustic leaching or other direct leaching e.g. Billiton process<sup>20-22</sup>, Atlair Process<sup>23,24</sup>, or alkaline leaching<sup>25,26</sup> can make lower energy extraction possible when compared to thermochemical and electrochemical extraction processes. Bulk and surface characterization of the extracted titania is critical in maximizing its phase purity and utilization. In this context, we investigate hydrometallurgical route of titania enrichment in Cox's Bazar Beach Sand. The aim is to obtain precursors that lead to nanocrystalline phase-pure anatase and mixed anatase/rutile composites as products for photocatalytic applications.

## 2. MATERIAL AND METHOD

### 2.1 Materials

Beach sand used in this study was supplied by Beach Sand Minerals Exploitation Center (BSMEC)<sup>27</sup>, Cox's Bazar, Bangladesh, in which rutile mineral of raw sand was previously beneficiated at BSMEC using physical separation steps<sup>28</sup> shown in Figure 1. This high-grade rutile-containing sand is referred to as 'As-received sand' throughout this article. Particle size of As-received sand ranged from 106 to 425  $\mu\text{m}$ . This sand was then ball milled for 5 minutes and a fraction below 212  $\mu\text{m}$  was retained for subsequent upgradation that followed the steps shown in Figure 2.

## 2.2 Methods

### 2.2.1 Hydrometallurgical upgradation

For upgradation (Figure 2), we used hydrometallurgical route involving hydrochloric acid leaching, digestion with sulfuric acid, water leaching, repetitive condensation, and dilution followed by drying and calcination. Acid leaching was carried out using a three-necked glass reactor connected with a reflux condenser along with a hot plate and magnetic stirrer. Initially, HCl leaching was conducted twice, in each, 20 w/w% of HCl solution in 1:6 w/v solid-liquid ratio at 110°C and a stirring speed of 400 rpm for 6 hours was used for leaching sand. The obtained slurry was cooled, filtered, and washed with 5 w/w% HCl and the residue was dried at 110°C overnight. The dried residue was used for H<sub>2</sub>SO<sub>4</sub> leaching using 80 w/w% H<sub>2</sub>SO<sub>4</sub> of 1:3 w/w solid-liquid ratio at 150°C for varying leaching times.

After completion of leaching, the slurry was diluted with water with a weight ratio of slurry to water at 1:1.5 following weighing the weight of the slurry. This water leaching was conducted for another 100 minutes at 75°C. The slurry was filtered, and the filtrate was condensed slowly at 110°C to evaporate water, the temperature was increased to its boiling point of about 300°C until blackish crystals appeared at the bottom of the flask. Dilution with distilled water caused white precipitation which was centrifuged, dried, and calcined at 900°C. All chemical reagents used were of analytical grade and distilled water was used throughout.

### 2.2.2 Morphology, Phase, and Surface Analyses

Morphological states of the minerals present in the as-received sand were imaged using polarizing microscopy (Model LEICA-ICC50E, Germany). The shape and color of mineral grains under plane-polarized and cross-polarized light were observed to identify minerals using the Michel-Levy color chart<sup>29</sup>. The phase purity of the as-received sand and the upgraded titania was analyzed using an X-ray diffractometer (XRD-Rigaku, Japan). Cu K<sub>α</sub> radiation of wavelength 0.154056 nm was used with a step size of 0.02 and a recorded range of 10-80 degrees. Rietveld refinement using X'pert HighScore Plus software was used to analyze probable phase concentration in the as-received sand and hydrometallurgically upgraded titania. Bulk chemistry was determined using X-ray Fluorescence (XRF, Model: Lab Center XRF-1800, SHIMADZU). The surface morphology and chemistry of the upgraded titania powder samples were analyzed using scanning electron microscopy (SEM, Model-EVO18 Research, Carl Zeiss, UK) equipped with an electron dispersive spectrometry (EDS, Model-EDAX, USA) for semi-quantitative elemental analysis. For analyzing elemental chemistry, X-ray photoelectron spectroscopy (XPS) was performed using a Kratos AXIS ULTRA spectrometer using Al K<sub>α</sub> radiation ( $h\nu = 1486.58$  eV) operated at 300W (20mA, 15kV). The spectra were calibrated with respect to the C 1s line at 284.8 eV.

## 3. RESULTS AND DISCUSSION

### 3.1 Morphological and Phase Analysis of As-received Sand

Figure 3 shows microscopic images of as received beach sand under the plane and cross-polarized light. Anisotropic minerals with moderate to strong birefringence show different interference colors in polarized light with different planes. With the help of Michel Levy interference color chart<sup>29</sup>, the interference color of minerals can be correlated with its actual retardation value, thickness, and birefringence, overall to identify the minerals<sup>30</sup>. As expected, the as-received beach sand showed a mixed nature with the presence of garnet (aluminosilicate), rutile, silica (SiO<sub>2</sub>), zircon (ZrSiO<sub>4</sub>), monazite (rare-earth phosphates), and chloritoid (iron magnesium manganese alumino-silicate hydroxide).

The mixed nature of the as-received sand is further confirmed by XRD (Figure 4). Phase analysis of the XRD pattern shows a mixture of garnet, ilmenite, hematite, rutile, silica, zircon, and silicates of Fe. Quantitative phase analysis using the Rietveld method (chi-square = 1.0367) estimated the presence of garnet, ilmenite, hematite and rutile as the dominant minerals (26, 19, 14 and 13 wt.% respectively) constituting over 70% of as received beach sand by weight.

Table 1 shows the chemical composition of the sand analyzed with XRF, along with the potential mineral sources from where the relevant chemistry could originate from based on the formula structure<sup>30</sup> or composition<sup>31</sup> following the lead from the polarizing microscopy and XRD.

Nearly 90% of the as-received sand is made of iron oxide, titania, silica/silicates and alumina/aluminates. Almost a quarter of this sand is a mixture of rutile titania and titania containing mineral ilmenite. This makes the Cox's Bazar beach sand an important sustainable source of titania.

Exact correspondence between the results from the three bulk characterization techniques namely polarisation microscopy, X-ray diffraction and X-ray Fluorescence of the as-received sand is neither possible nor was the target. Characterization information and detection limits, for example, of XRD and XRF are entirely different. So, while it may be possible to detect trace elements present in XRF data, it may not be possible to resolve any crystal phase presented by these elements if they are below the typical detection limit of XRD (~0.1%). The results presented in Figures 3 and 4, and Table 1 should be taken together as a broad representation of the morphology, phase mixture, and overall chemistry variations in the starting material. Assignments of potential mineral sources in Table 1 are, therefore, of indicative nature.

### 3.2 Hydrometallurgical enrichment of titania in Cox's Bazar Beach Sand

Having established the broad nature of the as received sand as a source of mainly titanium and iron-rich minerals (~64% by weight), we treated these sands hydrometallurgically using sulfuric acid (H<sub>2</sub>SO<sub>4</sub>) leaching varying the digestion time as a process variable between 45 and 135 minutes (Figure 2).

Figure 5a shows XRD patterns of the titania-enriched powders that were calcined from such digestion following water-leaching, condensation, dilution, filtration and drying. Interestingly, XRD patterns of calcined samples exhibit titania of anatase type as the predominant phase (denoted as A in Figure 5a) along with the presence of rutile phase (denoted as R). These samples were devoid of any iron, thus showing that the hydrometallurgical route was successful in enriching titania containing phases and eliminate iron and other impurities in the as received samples.

Noteworthy, diffractions from rutile phase titania becomes weaker as the digestion time increases to 60 (S60) and 90 (S90) minutes. A further increase of digestion time to 135 minutes, however, shows a reappearance of some of the rutile peaks (Figure 5a), with (110) plane of rutile appearing to be dominant. This appearance/reappearance of rutile phase is interesting as it means that the ratio between anatase and rutile can be tuned by varying the digestion times of during sulfuric acid leaching. We recall that commercially successful photocatalysts such as Aerodisp P25, Degussa, Germany is widely known to be an 80/20 mixture of anatase and rutile. We conducted Rietveld quantitative phase analysis using the XRD data obtained on these enriched samples. The data is presented in Table 2. The anatase to rutile phase ratio varied

between 77/23; 95/5, 100/0 and 84/16 for digestion times of 45, 60, 90 and 135 minutes respectively. The tunability of the relative amounts of anatase and rutile in the resulting calcined powders is shown in Figure 5b.

In addition to the tunability, XRD data was also used to estimate indicative size of the crystallites using Scherrer's formula<sup>32</sup>. Crystallite size generally varied between 40-70 nm (Table 2), with a maximum size of ~54 nm obtained for sample digested for 90 minutes (S90). Among the samples investigated in this study, this sample, S90 presented with the highest proportion of anatase along with the largest crystallite size. One can thus tune both the anatase/rutile ratio and the average crystallite size by controlling the digestion time. Further tunability of both the anatase/rutile ratio and the crystallite size is possible, as it is widely known, by varying the calcination time and temperature.

### 3.3 Surface morphology and chemistry of calcined powders of hydrometallurgically enriched titania

The nanocrystalline nature of the powder aggregates can be seen from the SEM images in Figure 6, which show a tendency of agglomeration of the particles in most of the samples of calcined powders. Agglomeration tendency and grain growth were found to be highest but regular for sample S90, which has been digested in sulfuric acid for 90 minutes. Agglomeration in sample S135 is somewhat similar to S90 albeit slightly smaller. Quicker digestion left with a smaller agglomerate size and a less uniform distribution in the size of the agglomerates.

Chemical analyses from EDS (Figure 6) show titanium and oxygen to dominate the spectra with minor impurities such as Fe, Si, P and S. Table 3 shows the semi-quantitative elemental composition of the SEM image areas. Samples S90 show relatively less proportion of impurities which may be responsible for its higher grain growth. The smaller size aggregate of S45 and S60 can be attributed to the relatively higher proportion of impurities, which may have worked as growth inhibitors during calcination.

During the calcination of amorphous meta-titanic acid, the presence of impurity can influence the polymorphic transformation temperature, phase concentration<sup>33,34</sup>, grain growth<sup>35</sup> and agglomerate size<sup>36-40</sup>. Within a certain range of concentration, some impurities can introduce a different type of defect resulting in accelerating or decelerating influence on anatase to rutile conversion rate<sup>33,34</sup>. Impurities of comparable size can form a solid solution, either increasing or decreasing defect concentration. Impurity<sup>36-38,41</sup> S, P, Si can inhibit the anatase to rutile transformation and grain growth<sup>34,40,42-45</sup>, among which P and Si have significant influence even at lower concentration<sup>34,37</sup>. In Table 3, the proportion of Si and P is higher in S45 and S60 compared to samples of longer digestion, which may explain their relatively smaller particle growth. On the other hand, the presence of Fe can both inhibit or promote the rutile formation<sup>33,46</sup> depending on its relative concentration. The lowest proportion of Fe in S90 may act as the reason behind obtaining the highest anatase phase in XRD analysis. However, the presence of multiple impurities with opposite influences makes it difficult to relate their synergistic effect based on semi-quantitative EDS analysis.

The reflectance data were recorded from UV-Vis spectroscopy. Later, the diffusive reflectance spectra were analyzed to calculate optical direct and indirect band gap using Kubelka-Munk formula<sup>47</sup> and Tauc plot, shown in Figure 6. While using this formula, following equation were used to calculate  $F(R_{\infty})$  and then  $(hvF(R_{\infty}))^2$  and  $(hvF(R_{\infty}))^{1/2}$  were plotted against  $hv$ . From the

intercept of the slope of the curves at  $h\nu$  axis, direct and indirect band gap were calculated, respectively.

$$F(R_{\infty}) = \frac{(1-R_{\infty})^2}{2R_{\infty}} \text{ where } R_{\infty} \text{ is the measured reflectance.}$$

As expected, the direct band gap energy is higher than the indirect band gap energy. Direct  $E_g$  is ranged from 3.24 eV to 3.34 eV, while the indirect one is ranged from 2.87 eV to 2.95 eV. According to Burstein–Moss effect<sup>48</sup>, widening of band gap energy occurs due to higher impurity concentration. The lowest band gap energy was observed for S90 while the highest was obtained for S60, which agrees with the impurity concentration found in the EDS data (Table 3).

The XPS survey spectrum of  $\text{TiO}_2$  powder extracted through 90 minutes digestion is shown in Figure 8, in which characteristic lines of titanium, oxygen, carbon, nitrogen and phosphorus is observed. While C and N can be present at the top surface as a common overlayers, the presence of P in XPS corresponds to the presence of P in the EDS data and may indicate that P can be an impurity present in both in the bulk as well as surface. The deconvolution of the Ti 2p XPS spectrum reveals the presence of two major bands with binding energies at 464.5 eV and 458.8 eV corresponding to the  $2p_{1/2}$  and  $2p_{3/2}$  components of  $\text{Ti}^{4+}$  in the  $\text{TiO}_2$  lattice<sup>49,50</sup>. The spin orbital splitting of 5.7 eV represents the  $\text{Ti}^{4+}$  from anatase Titania<sup>49,51,52</sup>. We will need further surface and interface analysis to establish a link between the optical and electron spectroscopic data. Irrespective of this lack of linkage, we observe that beach sands from Cox's Bazar can be successfully lead to photocatalysts composed of anatase and rutile of varying proportion through hydrometallurgical process.

#### 4. CONCLUSION

We have demonstrated that the hydrometallurgical route of titania enrichment in Cox's Bazar Beach Sand can produce precursors that can be conveniently converted into nanocrystalline phase-pure anatase and mixed anatase/rutile composites. The phase purity, crystallite size as well as morphology of the anatase can be tuned by varying digestion times. This route can be particularly important to produce high-performance nanocrystalline titania photocatalysts from a sustainable source of beach sand from Cox's Bazar of Bangladesh.

#### ACKNOWLEDGE

The authors gratefully acknowledge the support and facilities provided by Bangladesh Council of Scientific and Industrial Research (BCSIR), Bangladesh University of Engineering and Technology (BUET) and the European Commission Erasmus International Credit Mobility between BUET and University of Limerick, Ireland.

## REFERENCE

1. Lan Y, Lu Y, Ren Z. Mini review on photocatalysis of titanium dioxide nanoparticles and their solar applications. *Nano Energy*. 2013;2:1031-1045. doi:10.1016/j.nanoen.2013.04.002
2. Gambogi J. Titanium and titanium dioxide. *US Geol Surv ,Mineral Commod Summ*. 2022;(703). <https://pubs.usgs.gov/periodicals/mcs2022/mcs2022-titanium.pdf>
3. Zhang R, Elzatahry AA, Al-Deyab SS, Zhao D. Mesoporous titania: From synthesis to application. *Nano Today*. 2012;7(4):344-366. doi:10.1016/j.nantod.2012.06.012
4. Gambogi J. Titanium mineral concentrates. *US Geol Surv Miner Commod Summ*. 2022;(703). <https://pubs.usgs.gov/periodicals/mcs2022/mcs2022-titanium-minerals.pdf>
5. Gázquez MJ, Bolívar JP, Garcia-tenorio R, Vaca F. A Review of the Production Cycle of Titanium Dioxide Pigment. *Mater Sci Appl*. 2014;5:441-458. doi:<http://dx.doi.org/10.4236/msa.2014.57048>
6. Minkler WW, Baroch EF. The production of titanium, zirconium and hafnium. In: Tien JK, Elliott JF, eds. *Metallurgical Treatises*. AIME. ; 1981:171–189.
7. Akon E. Mineralogy , geochemistry and economic potentialities of heavy mineral sand resources of Bangladesh. 2019;59:1-8.
8. Bedinger GM. *2017 Minerals Yearbook*.; 2017.
9. Zhang W, Zhu Z, Cheng CY. A literature review of titanium metallurgical processes. *Hydrometallurgy*. 2011;108:177-188. doi:10.1016/j.hydromet.2011.04.005
10. Hoecker W. Process for the production of synthetic rutile. *United States Pat 5,601,630*. Published online 1997. <https://patentimages.storage.googleapis.com/b0/81/b8/4dc73ee04ff748/US5601630.pdf>
11. Sinha HN. Murso Process for Producing Rutile Substitute. In: Jaffee RI, Burte HM, eds. *Titanium Science and Technology*. Springer; 1973:233-245. doi:[https://doi.org/10.1007/978-1-4757-1346-6\\_18](https://doi.org/10.1007/978-1-4757-1346-6_18)
12. Robinson M, Clamp F, Aberdeen D, Barry Mobbs D. Beneficiation of Ilmenite Ores. Published online 1975. <https://www.freepatentsonline.com/3897537.pdf>
13. Walpole EA, Winter D. The Austpac ERMS and EARS Processes for the Manufacture of High-Grade Synthetic Rutile by the Hydrochloric Acid Leaching of Ilmenite. In: *International Conference on the Practice and Theory of Chloride/Metal Interaction*. ; 2002:1-14. <https://www.austpacresources.com/pdfs/techpub/EJW Paper Oct 2002.pdf>
14. Kahn JA. Non-Rutile Feedstocks for the Production of Titanium. *JOM*. 1984;36:33-38. doi:<https://doi.org/10.1007/BF03338498>
15. Kataoka S, Yamada S. Acid leaching upgrades ilmenite to synthetic rutile. *Chem Eng*. 1973;80(7):92-93. [https://www.researchgate.net/publication/284686886\\_Acid\\_leaching\\_upgrades\\_ilmenite\\_to\\_synthetic\\_rutile/stats](https://www.researchgate.net/publication/284686886_Acid_leaching_upgrades_ilmenite_to_synthetic_rutile/stats)
16. Nguyen TH, Lee MS. A review on the recovery of titanium dioxide from Ilmenite ores by direct leaching technologies. *Miner Process Extr Metall Rev*. 2018;00(00):1-17. doi:10.1080/08827508.2018.1502668
17. Xiong X, Wang Z, Wu F, Li X, Guo H. Preparation of TiO<sub>2</sub> from ilmenite using sulfuric acid decomposition of the titania residue combined with separation of Fe<sup>3+</sup> with EDTA during hydrolysis. *Adv Powder Technol*. 2013;24:60-67. doi:10.1016/j.appt.2012.02.002
18. Li Z, Wang Z, Li G. Preparation of nano-titanium dioxide from ilmenite using sulfuric acid-decomposition by liquid phase method. *Powder Technol*. 2016;287:256-263. doi:10.1016/j.powtec.2015.09.008

19. Jia L, Liang B, Lü L, et al. Beneficiation of titania by sulfuric acid pressure leaching of Panzhihua ilmenite. *Hydrometallurgy*. 2014;150:92-98. doi:10.1016/j.hydromet.2014.09.016
20. Roche EG, Stuart AD, Grazier PE. Production of Titania. Published online 2004. <https://patentimages.storage.googleapis.com/aa/31/3c/83e84c8e72e372/WO2004035841A1.pdf>
21. Roche EG, Stuart AD, Grazier PE, Nicholson S. Production of Titania. Published online 2005.
22. Stuart AD, Lawson JA, Ward CB, Peng H. A sulphate process. Published online 2010.
23. Verhulst D, Sabacky B, Spitler T, Duyvesteyn W. The Altair TiO<sub>2</sub> pigment process and its extension into the field of nanomaterials. *CIM Bull*. 2002;95(1065):89-94. [https://www.researchgate.net/publication/283878971\\_The\\_Altair\\_TiO2\\_pigment\\_process\\_and\\_its\\_extension\\_into\\_the\\_field\\_of\\_nanomaterials](https://www.researchgate.net/publication/283878971_The_Altair_TiO2_pigment_process_and_its_extension_into_the_field_of_nanomaterials)
24. Verhulst D, Sabacky B, Spitler T, Duyvesteyn W. New developments in the Altair hydrochloride TiO<sub>2</sub> pigment process. *Hydrometallurgy 2003, 5th Int Conf Honor Prof R Ritchie, Vancouver, August 2003*. 2003;1:565-575. [https://www.researchgate.net/publication/237307472\\_New\\_developments\\_in\\_the\\_Altair\\_TiO2\\_hydrochloride\\_pigment\\_process](https://www.researchgate.net/publication/237307472_New_developments_in_the_Altair_TiO2_hydrochloride_pigment_process)
25. Nayl AA, Awwad NS, Aly HF. Kinetics of acid leaching of ilmenite decomposed by KOH. Part 2. Leaching by H<sub>2</sub>SO<sub>4</sub> and C<sub>2</sub>H<sub>2</sub>O<sub>4</sub>. *J Hazard Mater*. 2009;168:793-799. doi:10.1016/j.jhazmat.2009.02.076
26. Editorial G. Titanium and iron dissolutions from ilmenite by acid leaching and microbiological oxidation techniques. *ASIA-PACIFIC J Chem Eng*. 2013;8:323–330. doi:10.1002/apj.1663
27. Beach Sand Minerals Exploitation Center. <http://www.baec.gov.bd/site/page/7b3c53af-1472-4efd-a1b6-9a1bffa8266/->
28. Akash FA. *Beach Sand Minerals Exploitation Center ( BSMEC )*.; 2020. doi:10.13140/RG.2.2.28233.29287
29. Engineering MR, Seelandsveg S. A revised Michel-Le´vy interference colour chart based on first-principles calculations. 2013;(September 2012):5-10. doi:10.1127/0935-1221/2013/0025-2252
30. A. Mange M, F.W. Maurer H. *Heavy Minerals in Colour*. 1st ed. Chapman & Hall; 1992. doi:10.1016/0037-0738(92)90064-x
31. Akon E. Mineralogy, geochemistry and economic potentialities of heavy mineral sand resources of Bangladesh. *J Nepal Geol Soc*. 2019;59:1-8. doi:10.3126/jngs.v59i0.24981
32. Bashar MS, Matin R, Sultana M, et al. Effect of rapid thermal annealing on structural and optical properties of ZnS thin films fabricated by RF magnetron sputtering technique. *J Theor Appl Phys*. 2020;14(1):53-63. doi:10.1007/s40094-019-00361-5
33. Paul TC, Babu MH, Podder J, Dev BC, Sen SK, Islam S. Influence of Fe<sup>3+</sup> ions doping on TiO<sub>2</sub> thin films: Defect generation, d-d transition and band gap tuning for optoelectronic device applications. *Phys B Condens Matter*. 2021;604:412618. doi:10.1016/j.physb.2020.412618
34. Zhang YH, Reller A. Investigation of mesoporous and microporous nanocrystalline silicon-doped titania. *Mater Lett*. 2003;57(24-25):4108-4113. doi:10.1016/S0167-577X(03)00345-8
35. Gallardo Amores JM, Sanchez Escribano V, Busca G. Anatase crystal growth and phase transformation to rutile in high-area TiO<sub>2</sub>, MoO<sub>3</sub>-TiO<sub>2</sub> and other TiO<sub>2</sub>-supported oxide catalytic systems. *J Mater Chem*. 1995;5(8):1245-1249. doi:10.1039/JM9950501245

36. Grzmil B, Kic B, Rabe M. Inhibition of the anatase - Rutile phase transformation with addition of K<sub>2</sub>O, P<sub>2</sub>O<sub>5</sub>, and Li<sub>2</sub>O. *Chem Pap*. 2004;58(6):410-414.
37. Criado J, Real C. Mechanism of the inhibiting effect of phosphate on the anatase → rutile transformation induced by thermal and mechanical treatment of TiO<sub>2</sub>. *J Chem Soc Faraday Trans 1 Phys Chem Condens Phases*. 1983;79(12):2765-2771. doi:10.1039/F19837902765
38. Gesenhues U. Calcination of metatitanic acid to titanium dioxide white pigments. *Chem Eng Technol*. 2001;24(7):685-694. doi:10.1002/1521-4125(200107)24:7<685::AID-CEAT685>3.0.CO;2-1
39. Hanaor DAH, Sorrell CC. Review of the anatase to rutile phase transformation. *J Mater Sci*. 2011;46(4):855-874. doi:10.1007/s10853-010-5113-0
40. Kaur T, Sraw A, Wanchoo RK, Toor AP. Visible -Light Induced Photocatalytic Degradation of Fungicide with Fe and Si Doped TiO<sub>2</sub> Nanoparticles. *Mater Today Proc*. 2016;3(2):354-361. doi:10.1016/j.matpr.2016.01.020
41. Okada K, Yamamoto N, Kameshima Y, Yasumori A, MacKenzie KJD. Effect of Silica Additive on the Anatase-to-Rutile Phase Transition. *J Am Ceram Soc*. 2001;84(7):1591-1596. doi:10.1111/j.1151-2916.2001.tb00882.x
42. Majeed Khan MA, Siwach R, Kumar S, Alhazaa AN. Role of Fe doping in tuning photocatalytic and photoelectrochemical properties of TiO<sub>2</sub> for photodegradation of methylene blue. *Opt Laser Technol*. 2019;118(March):170-178. doi:10.1016/j.optlastec.2019.05.012
43. Wu D, Mao F, Yang Z, Wang S, Zhou Z. Silicon and aluminum co-doping of titania nanoparticles: Effect on thermal stability, particle size and photocatalytic activity. *Mater Sci Semicond Process*. 2014;23(1):72-77. doi:10.1016/j.mssp.2014.02.040
44. Wang Y, Li J, Peng P, Lu T, Wang L. Preparation of S-TiO<sub>2</sub> photocatalyst and photodegradation of L-acid under visible light. *Appl Surf Sci*. 2008;254(16):5276-5280. doi:10.1016/j.apsusc.2008.02.050
45. Mohamed RM, Aazam E. Synthesis and characterization of P-doped TiO<sub>2</sub> thin-films for photocatalytic degradation of butyl benzyl phthalate under visible-light irradiation. *Cuihua Xuebao/Chinese J Catal*. 2013;34(6):1267-1273. doi:10.1016/S1872-2067(12)60572-5
46. IIDA Y, OZAKI S. Grain Growth and Phase Transformation of Titanium Oxide During Calcination. *J Am Ceram Soc*. 1961;44(3):120-127. doi:10.1111/j.1151-2916.1961.tb13725.x
47. Hossain MS, Akter Y, Shahjahan M, et al. Influence of Ni substitution on structural, morphological, dielectric, magnetic and optical properties of Cu-Zn ferrite by double sintering sol-gel technique. *J Adv Dielectr*. 2019;9(2). doi:10.1142/S2010135X19500206
48. Munir S, Mujtaba S, Hussain H, Ali R. Effect of carrier concentration on the optical band gap of TiO<sub>2</sub> nanoparticles. *JMADE*. 2016;92:64-72. doi:10.1016/j.matdes.2015.12.022
49. Nasir M, Zhang J, Chen F, Tian B. Detailed study of Ce and C codoping on the visible light response of titanium dioxide. *Res Chem Intermed*. 2015;41(3):1607-1624. doi:10.1007/s11164-013-1297-7
50. Moulder JF, Stickle WF, Sobol PE, Bomben KD. Handbook of X-ray Photoelectron Spectroscopy Edited by. *Google Sch*. Published online 1993:1-261. [https://books.google.com/books/about/Handbook\\_of\\_X\\_ray\\_Photoelectron\\_Spectros.html?hl=fr&id=A\\_XGQgAACAAJ](https://books.google.com/books/about/Handbook_of_X_ray_Photoelectron_Spectros.html?hl=fr&id=A_XGQgAACAAJ)
51. Power A, Efficiencies C, Chen D, et al. Dye-Sensitized Solar Cells Employing a. *ACS Nano*. 2010;4(8):4420-4425.

52. Silversmit G, De Doncker G, De Gryse R. A Mineral TiO<sub>2</sub>(001) Anatase Crystal Examined by XPS. *Surf Sci Spectra*. 2002;9(1):21-29. doi:10.1116/11.20020701

Accepted Article

Table 1: Chemical Composition of the As-received Sand from XRF.

Analyte (Potential mineral source)	Mass, wt.%	Analyte (Potential mineral source)	Mass, wt.%
Fe <sub>2</sub> O <sub>3</sub> (Hematite/ Ilmenite/Garnet/ Chloritoid/ Hornblende)	42.50	ZrO <sub>2</sub> (Zircon)	0.608
TiO <sub>2</sub> (Rutile/Ilmenite)	21.40	CeO <sub>2</sub> (Monazite)	0.591
SiO <sub>2</sub> (Silica/Garnet/Zircon/ Chloritoid/ Hornblende)	16.70	P <sub>2</sub> O <sub>5</sub> (Monazite)	0.380
Al <sub>2</sub> O <sub>3</sub> (Garnet/ Chloritoid/ Hornblende)	8.14	Nd <sub>2</sub> O <sub>3</sub> (Monazite)	0.300
CaO (Garnet/Hornblende)	2.13	ThO <sub>2</sub> (Monazite)	0.280
Cr <sub>2</sub> O <sub>3</sub> (Garnet)	1.92	La <sub>2</sub> O <sub>3</sub> (Monazite)	0.264
MgO (Chloritoid/Hornblende)	1.71	Na <sub>2</sub> O (Hornblende)	0.227
MnO (Garnet/Chloritoid)	1.08	Nb <sub>2</sub> O <sub>5</sub> (Rutile)	0.211
K <sub>2</sub> O (Silicates)	0.911	Y, S, Ni, Rb, Sr, Sn, Sm, Pb, U (impurities from unknown sources)	0.654

Table 2: A quantitative phase analysis of hydrometallurgically enriched titania in Cox's Bazar beach-sand.

Digestion time (minutes)	Rutile Titania wt.%	Anatase titania wt.%	Rietveld Refinement R-Parameters			Average crystallite size (nm)		
			$\chi^2$	R <sub>p</sub>	R <sub>wp</sub>	Mixed aggregate	Rutile	Anatase
45	23.1	76.9	1.186	0.0395	0.0560	49.0	67.4	39.8
60	5.4	94.6	1.375	0.0443	0.0667	43.6	47.2	42.7
90	0.0	100.0	1.249	0.0642	0.0916	53.9	0.0	53.9
135	15.9	84.1	1.162	0.0644	0.0950	41.8	46.0	39.7

Table 3: Semi-quantitative elemental composition from EDS of titania powders

Element	Average weight %			
	45 min	60 min	90 min	135 min
Ti	33.90	49.00	55.76	38.95
O	60.40	40.20	42.32	54.92
Fe	2.24	0.83	0.55	0.69
Si	0.60	0.66	0.34	0.28
P	2.10	1.92	0.96	0.95
S	0.81	7.42	0.07	4.21

le

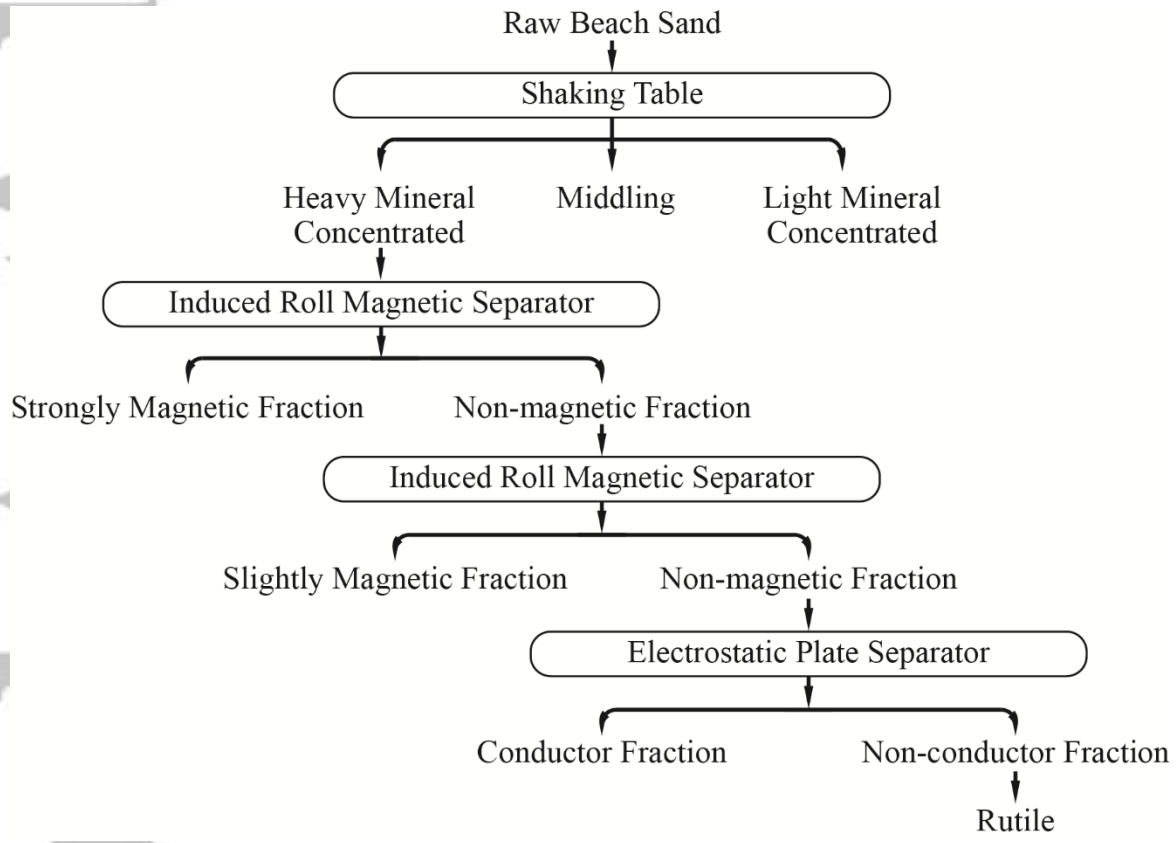


Figure 1: Beneficiation History of As-received Beach Sand (from Reference [28]).

Accepted

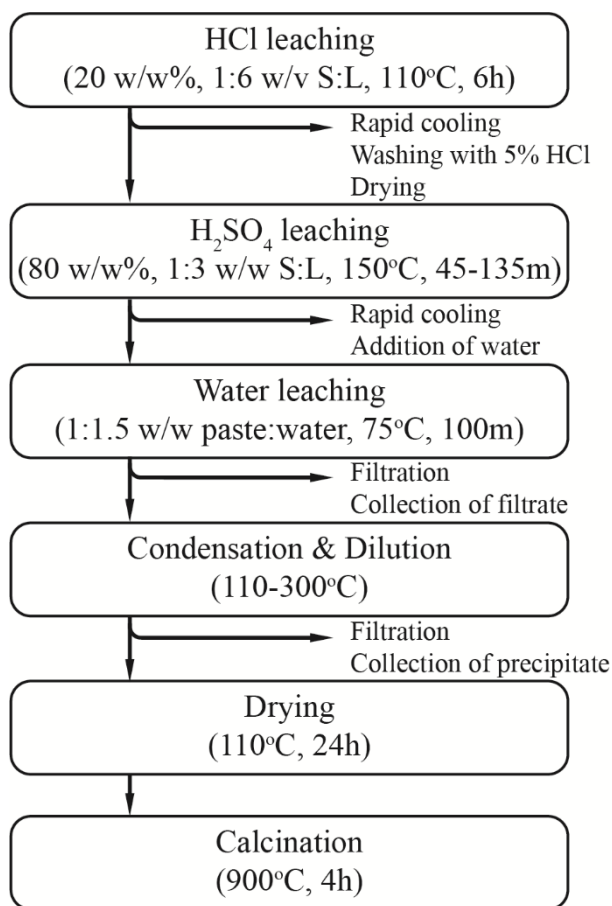


Figure 2: Flowchart of the upgradation process

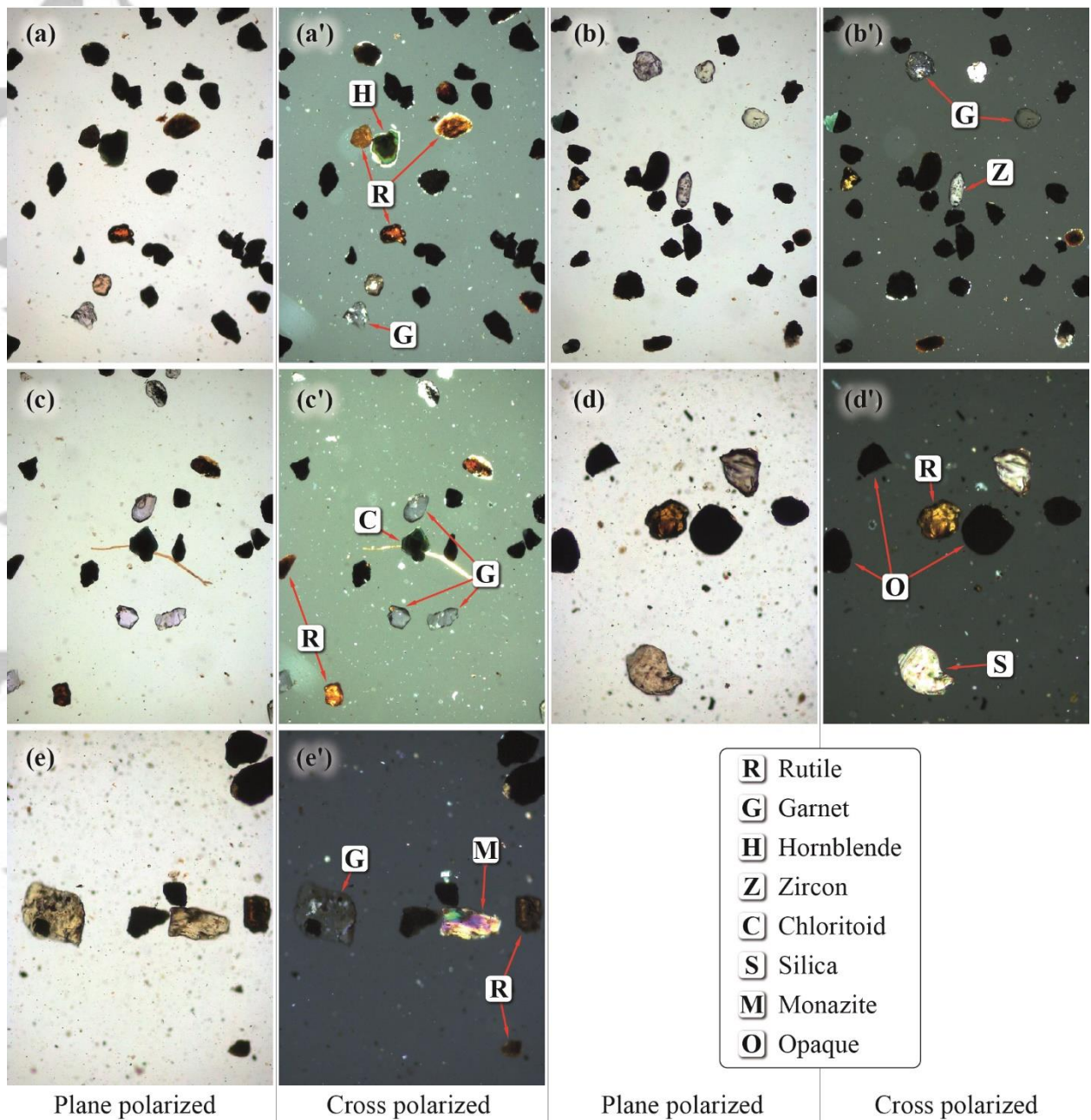


Figure 3: Polarizing Microscopic images of as-received sand using plane polarized light (a, b, c, d, e) and cross polarized light (a', b', c', d', e') identifying particles of (a') garnet, rutile, hornblende, (b') garnet, zircon (c') rutile, chloritoid, garnet, (d') silica, rutile, and (e') monazite, rutile, garnet

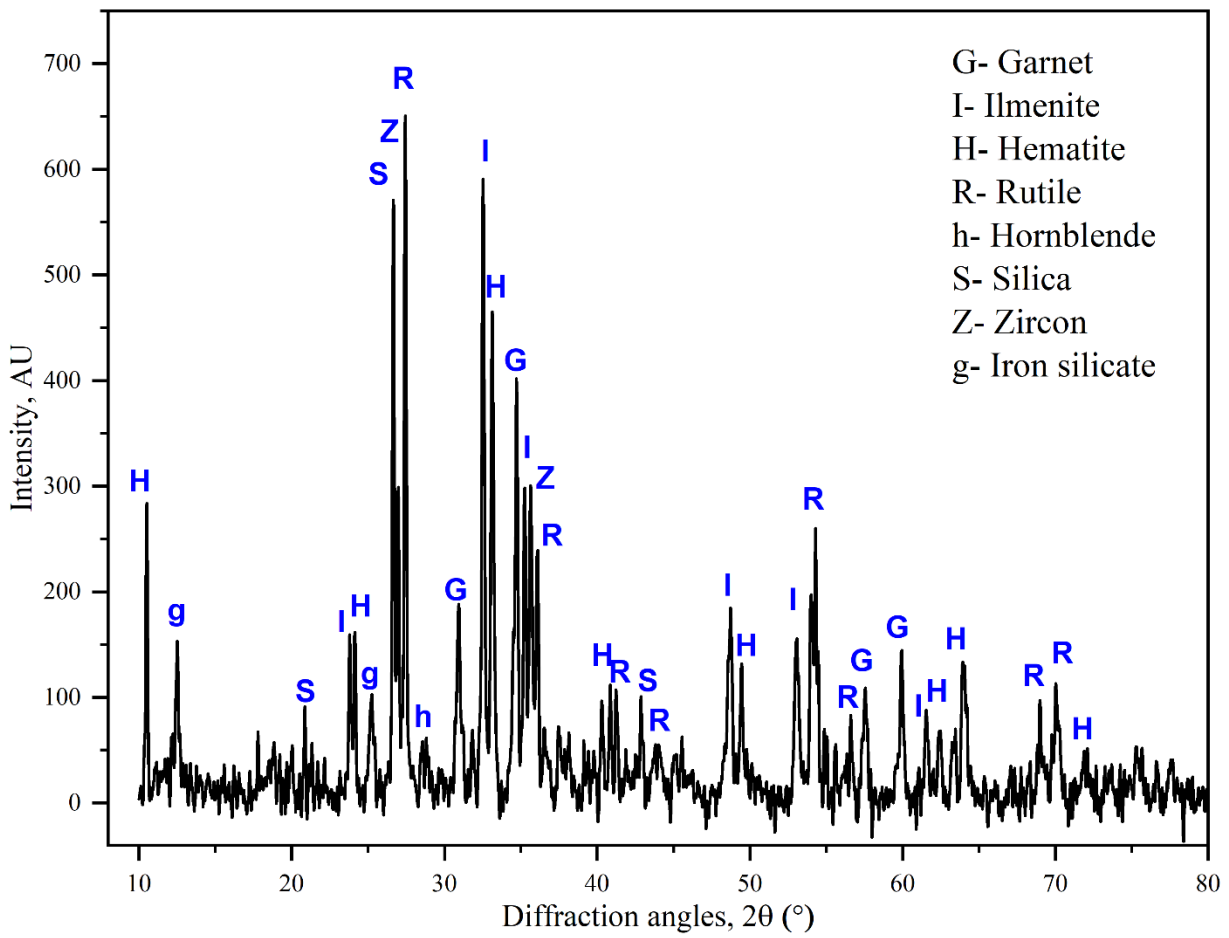


Figure 4: XRD pattern of as-received sand

Accept

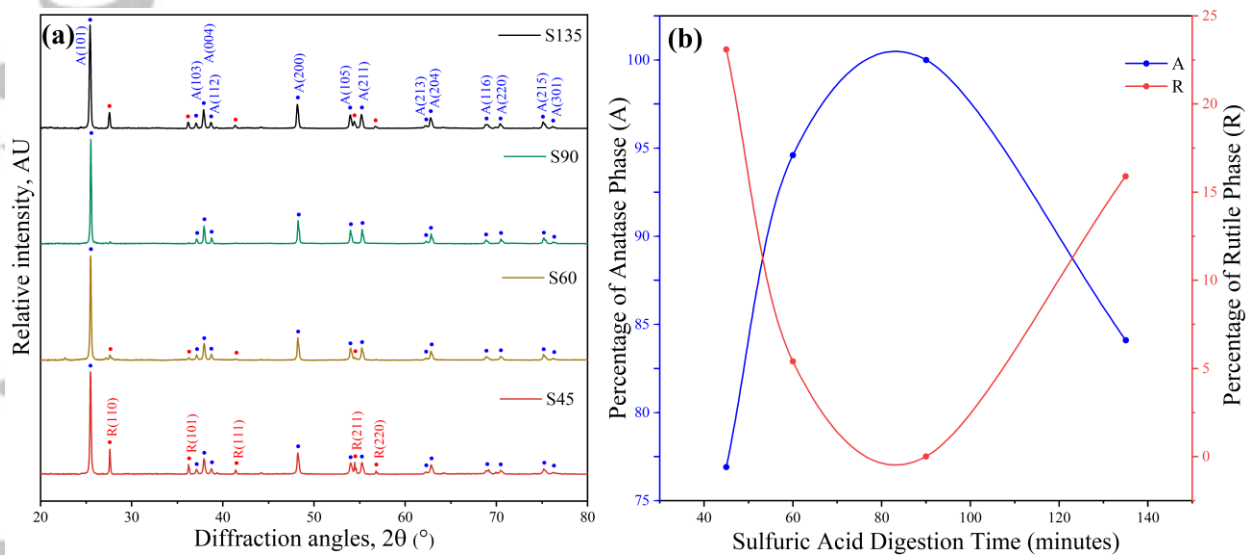


Figure 5: (a) X-ray Diffraction phase analysis of hydrometallurgically enriched titania powder (calcined at 900°C) obtained through varying digestion time in sulfuric acid: anatase (A) and rutile (R); b) relative distribution of anatase and rutile phases in these powders obtained from quantitative phase analyses using Rietveld method (Table 2).

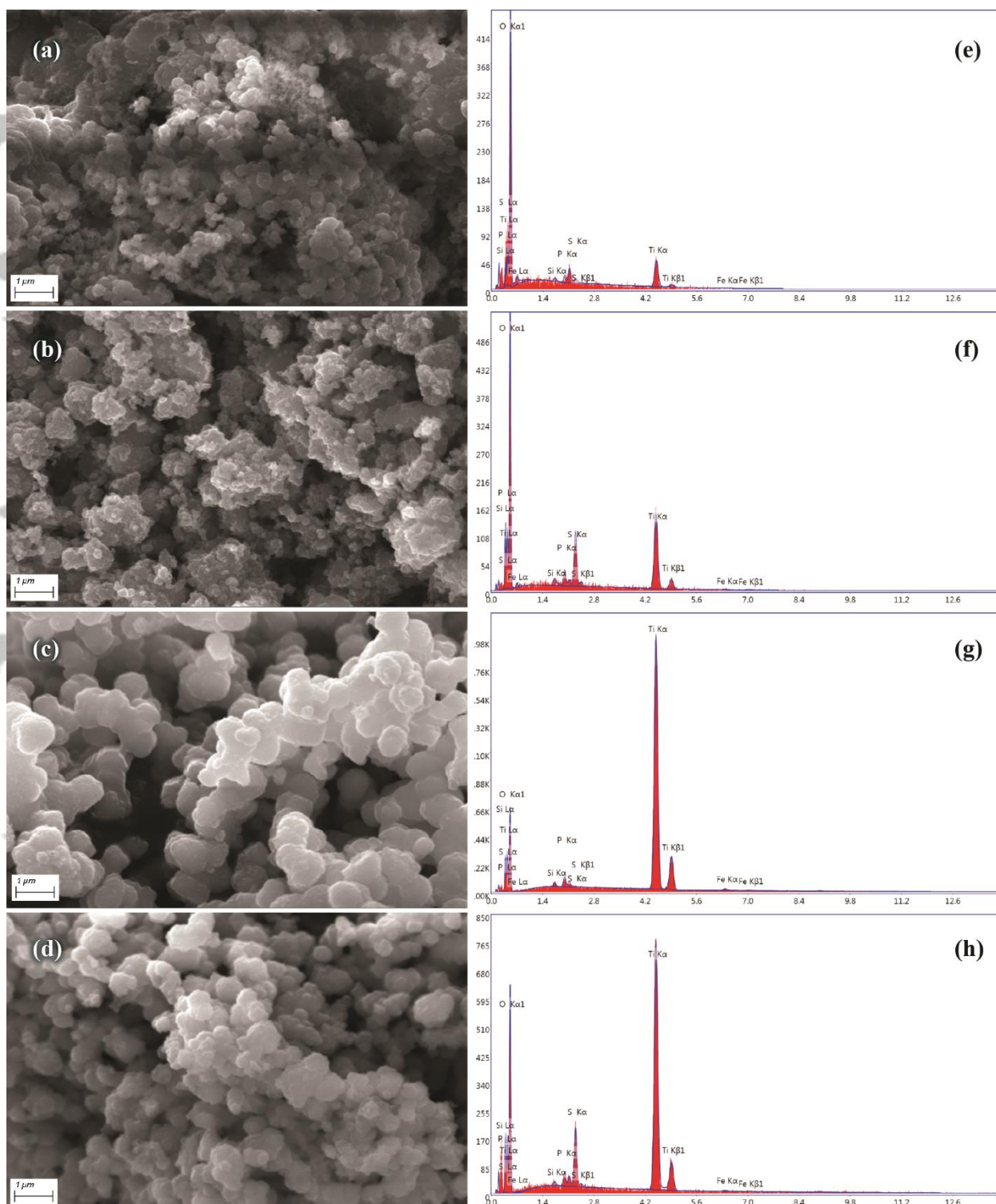


Figure 6: SEM images of titania obtained for different  $H_2SO_4$  digestion times of (a) 45min, (b) 60 min, (c) 90min, and (d) 135min and EDS spectra for different  $H_2SO_4$  digestion times of (e) 45min, (f) 60 min, (g) 90min, and (h) 135min

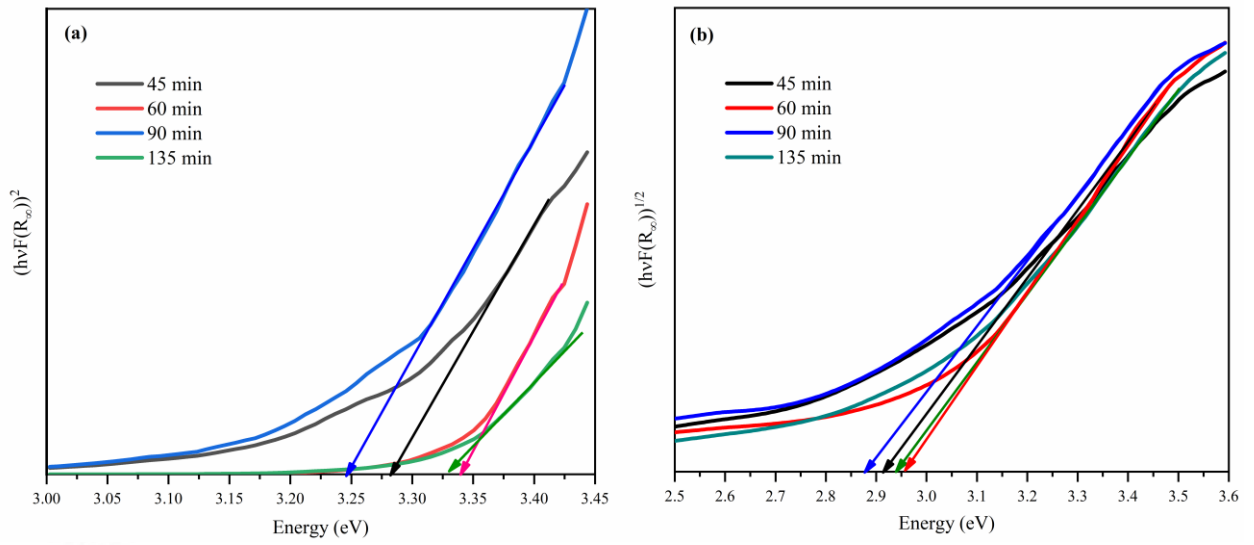


Figure 7: Kubelka-Munk transformed reflectance spectra of TiO<sub>2</sub> powders

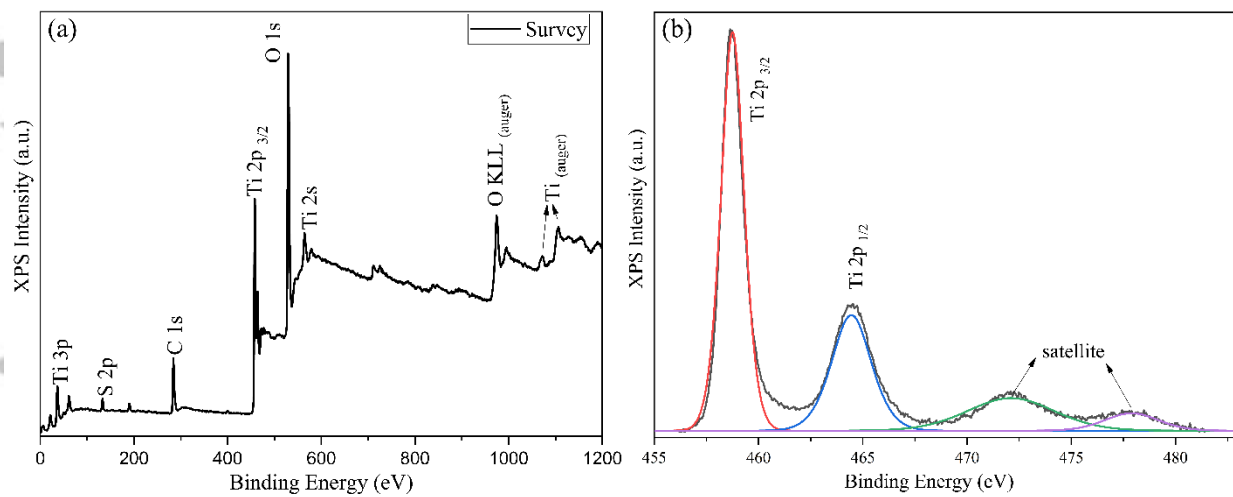


Figure 8: (a) XPS survey spectra of TiO<sub>2</sub> powder (90 minutes digested) showing elemental composition (b) deconvoluted high resolution Ti 2p peaks.